

Geometrically consistent static aeroelastic simulation using isogeometric analysis

Gillebaart, E.; De Breuker, R.

DOI

[10.1016/j.cma.2018.05.033](https://doi.org/10.1016/j.cma.2018.05.033)

Publication date

2018

Document Version

Final published version

Published in

Computer Methods in Applied Mechanics and Engineering

Citation (APA)

Gillebaart, E., & De Breuker, R. (2018). Geometrically consistent static aeroelastic simulation using isogeometric analysis. *Computer Methods in Applied Mechanics and Engineering*, 340, 296-319. <https://doi.org/10.1016/j.cma.2018.05.033>

Important note

To cite this publication, please use the final published version (if applicable). Please check the document version above.

Copyright

Other than for strictly personal use, it is not permitted to download, forward or distribute the text or part of it, without the consent of the author(s) and/or copyright holder(s), unless the work is under an open content license such as Creative Commons.

Takedown policy

Please contact us and provide details if you believe this document breaches copyrights. We will remove access to the work immediately and investigate your claim.

Geometrically consistent static aeroelastic simulation using isogeometric analysis

E. Gillebaart*, R. De Breuker

Department of Aerospace Structures and Materials, Faculty of Aerospace Engineering, Delft University of Technology, Netherlands

Received 30 August 2017; received in revised form 8 April 2018; accepted 27 May 2018

Available online 2 June 2018

Abstract

In conventional aeroelastic analysis and optimisation methods for wing design, different geometries are used for the different steps in the process. Generally, a parametrised model is used to describe the shape of the geometry for the optimisation process. Subsequently, this model is converted into a structural and aerodynamic model for analysis purposes. These steps increase the computational effort and introduce geometrical errors. In this work, a geometrically consistent static aeroelastic analysis framework is presented. By using isogeometric analysis, the exact geometry is used in both the structural and aerodynamic models, preventing any additional computational effort for meshing and geometry retrieval steps and avoiding the introduction of geometrical errors due to the discretisation of the geometry. The separate components of the framework are described and verified, and the complete framework is demonstrated through the analysis of the realistic wing model.

© 2018 Elsevier B.V. All rights reserved.

Keywords: Isogeometric analysis; Aeroelasticity; Potential flow theory; Reissner–Mindlin theory; Shell-BEM coupling

1. Introduction

With the trend of aircraft wings becoming more slender and flexible, the need for multidisciplinary analysis and optimisation is becoming more and more essential. The two main disciplines, aerodynamic and structural analysis, should be taken into account simultaneously to enable crucial trade-offs between the two disciplines. This will allow for improved overall performance of the future aircraft. Furthermore, goals set out by European programs like Flightpath 2050 [1] are challenging to achieve with current aircraft configurations. Deviation of the well-known “wing and tube” configuration will render large portions of the empirical data and knowledge currently used in aircraft design obsolete. Physics-based models can be used to bridge this gap and enable the design of new aircraft concepts.

The benefit of combining aerodynamics and structures in the analysis and optimisation of aircraft wings has been explored extensively in the last 40 years. An overview of earlier work can be found in the review article by Sobieszcwanski-Sobieski and Haftka [2]. In more recent years there has been more emphasis on including high-fidelity

* Correspondence to: Kluiverweg 1, 2629 HS Delft, The Netherlands.

E-mail address: e.gillebaart@tudelft.nl (E. Gillebaart).

models in the aerostructural optimisation routines. Kenway and Martins [3] used large-scale parallel computational power to perform aerostructural optimisation using an Euler aerodynamic model and a finite element shell structural model. The free form deformation (FFD) method was used to generate a parametrisation for the geometry. A similar level of fidelity was used in the work of Zhang et al. [4], who demonstrated a different way of parametrising the geometry using B-spline surface patches. The FFD parametrisation was also used by Brooks et al. [5] who increased the fidelity of the aerodynamic analysis to a Reynolds-averaged Navier–Stokes (RANS) model to perform aerostructural optimisation of a tow-steered composite wing.

The high-fidelity models are computationally expensive and are thus not suitable to explore larger areas of the design space. For preliminary design, lower-fidelity models are therefore still required. Recent work of Elham and Van Tooren [6] presents an aerostructural optimisation using a panel method coupled to a beam model. A quasi-3D boundary layer analysis is used to compute the viscous drag. The geometry was parametrised using Chebychev polynomials. Kennedy and Martins [7] demonstrated an optimisation framework consisting of a panel method and a shell finite element model and the FFD parametrisation method.

All the work that is mentioned here shares the same general layout of the computational frameworks. A parametrisation of the geometry is created to be able to efficiently describe and modify the shape and layout of the aircraft wing. This geometry is subsequently converted or translated to analysis-suitable geometries for the aerodynamic and structural analyses. This step can be computationally expensive and, moreover, introduce errors due to the approximative nature of conventional aerodynamic and structural models [8]. These errors could result in spurious local minima when performing shape optimisation, or may even, depending on the robustness of the meshing algorithm, cause the optimisation routine to fail when exploring the design space far away from the initial solution. Additionally, the possible shapes of the geometry are often limited depending on the chosen parametrisation.

Isogeometric analysis (IGA), as introduced by Hughes et al. [9], was recognised from the start to have the potential to overcome these issues in shape optimisation [10]. The principle of isogeometric analysis is to use the same underlying functions that are used in computer aided design (CAD) programs to describe the geometry, such as non-uniform rational b-splines (NURBS) or T-splines, to describe both the geometry and the unknown fields in the analysis process. This removes the geometry conversion step and guarantees that the exact geometry is used at all time. The added benefit in shape optimisation is that the CAD description in itself is a convenient and efficient parametrisation of the shape, which can directly be used in optimisation and enables a considerable, but smooth, variation in shape.

Application of IGA in shape optimisation processes has already been explored extensively in many different disciplines such as elasticity [11–13], hydrodynamics [14], fluid–structure interaction (FSI) [15,16], or thermodynamics [17]. In the field of aeroelasticity, the application of IGA is limited. Analysis of wind turbine blades using a IGA shell model and IGA incompressible Navier–Stokes aerodynamics was performed by Bazilevs et al. [18,19]. Ferede et al. [20] used the concept for the parametrisation of the geometry and the discretisation of the beam model that represents the turbine blade structure. The authors of the present work already presented a 2D aeroelastic analysis and optimisation framework, which was used for optimisation of a morphing airfoil [21].

The present work is a further development of the 2D isogeometric aeroelastic analysis from previous work and describes a geometrically consistent aeroelastic framework for the analysis of 3D aircraft wings. The IGA concept is used to ensure that the exact geometry is used in both the Reissner–Mindlin shell model and the potential flow aerodynamic boundary element model. These models were selected for their appropriate fidelity-level for preliminary design and their natural combination with the isogeometric concept. CAD software generally delivers a description of the boundary of the geometry, which is precisely what both the structural and aerodynamic models under consideration require. The two models are closely coupled through a radial-basis function (RBF) interpolation routine, and in a post-processing step, the structural strength and buckling and the aerodynamic viscous drag are computed.

In Section 2 of this paper, the computational models and techniques are described, and their implementations are verified against reference solutions. In the next section, the analysis of a realistic 3D wing demonstrates the capabilities of the framework. Three load cases are analysed, and the results are discussed. Finally, conclusions are drawn about the presented framework.

2. Computational techniques

The isogeometric aeroelastic analysis method presented in this paper consists of four distinct modules that interact with each other to find the final aeroelastic result. In Fig. 1, an overview of the complete method with the internal interactions is presented to get a better understanding of how the model is assembled.

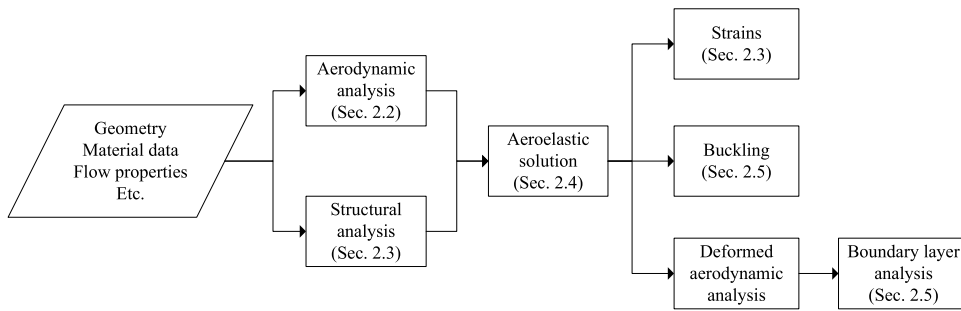


Fig. 1. Overview of the isogeometric aeroelastic analysis framework.

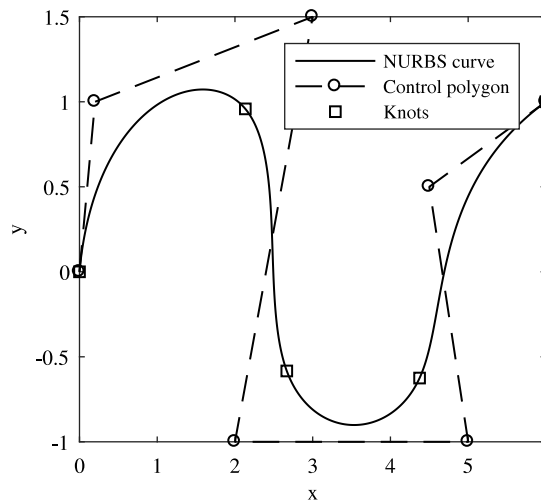


Fig. 2. Example of a NURBS curve with control polygon and knot location.

The main modules are the aerodynamic and structural ones, which are described in Sections 2.2 and 2.3. These models are coupled to each other to enable the computation of the aeroelastic equilibrium, as explained in Section 2.4. The results from this aeroelastic analysis are used to compute the strains (Section 2.3), the buckling behaviour (Section 2.5) and the viscous drag of the aeroelastically deformed geometry (Section 2.5). First, a short overview of the isogeometric principle, which is used in most of the modules, is given in Section 2.1.

2.1. Isogeometric analysis concept

The principle of IGA, introduced in 2005 [9], is to apply basis functions that are typically used in CAD to the analysis as well, for which usually conventional polynomial basis functions are used. In the present work, NURBS basis functions are used, because these are the most common in CAD software despite many developments within the isogeometric analysis research field, such as T-splines [22]. A NURBS curve is fully defined by four items:

- The control points $\mathbf{P}_i \in \mathbb{R}^d$, $1 \leq i \leq n$, where d indicates the dimensionality of the problem and n the number of control points.
- The weights w_i assigned to every control point.
- The degree p of the basis functions.
- The knot vector $\Xi = [\xi_1, \xi_2, \dots, \xi_{n+p+1}]$.

To simplify the explanation an example of a two-dimensional NURBS curve of degree 3 is shown in Fig. 2. This example shows that the control points may or may not be on the curve. Only so-called open knot vectors are used in

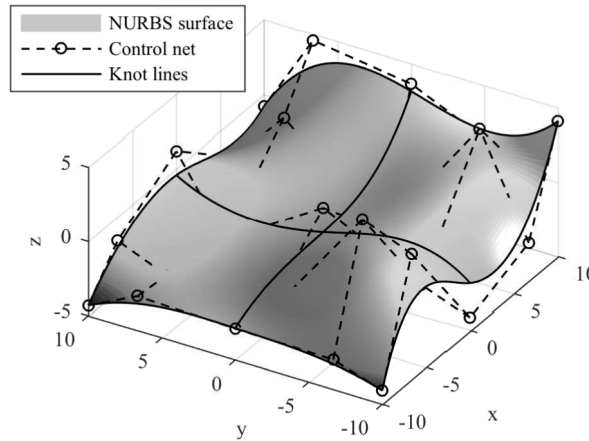


Fig. 3. Example of a NURBS surface with control net and knot locations.

the present work, meaning that the first and last knots are repeated $p + 1$ times. As a consequence, the NURBS curve is always interpolatory at the start and end of the curve. The order of continuity of the rest of the curve can be modified by repeating the other knots. The order of continuity at a knot is equal to $p + 1 - r$, where r is the multiplicity of this knot.

Mathematically, a NURBS curve can be represented as follows:

$$C(\xi) = \sum_{i=1}^n R_{i,p}(\xi)P_i \tag{1}$$

where $C(\xi)$ is the vector with Cartesian coordinates of the point described by the parametric point $\xi_1 \leq \xi \leq \xi_{n+p+1}$, and $R_{i,p}(\xi)$ is the i th rational basis functions of degree p . These basis functions are given by

$$R_{i,p}(\xi) = \frac{N_{i,p}(\xi)w_i}{\sum_{j=1}^n N_{j,p}(\xi)w_j} \tag{2}$$

where $N_{i,p}(\xi)$ is a B-spline basis function of order p , and w_i is the weight factor corresponding to the i th control point. The B-spline basis functions of degree 0 are defined as

$$N_{a,0}(\xi) = \begin{cases} 1 & \text{if } \xi_i \leq \xi \leq \xi_{i+1} \\ 0 & \text{otherwise} \end{cases} \tag{3}$$

and for higher degrees

$$N_{i,p}(\xi) = \frac{\xi - \xi_i}{\xi_{i+p} - \xi_i} N_{i,p-1}(\xi) + \frac{\xi_{i+p+1} - \xi}{\xi_{i+p+1} - \xi_{i+1}} N_{i+1,p-1}(\xi) \tag{4}$$

The recursive character results in higher cost for computing the basis functions. However, several efficient algorithms exist to speed up the computations, of which the Cox–de-Boor algorithm [23] is most popular. This algorithm was therefore also used in this work.

NURBS basis functions (as well as B-spline basis functions) possess some properties that are favourable for their implementation into analysis models. The basis functions possess the local support property, meaning that in every knot span $[\xi_i, \xi_{i+1})$ at most $p + 1$ non-zero basis functions exist, namely $N_{i-p,p}, \dots, N_{i,p}$. Furthermore, they are non-negative and form a partition of unity at each parametric location. In the interior of the knot span, all derivatives of the non-zero basis functions exist, and at a knot itself, the functions are $p - r$ times continuously differentiable.

The same principles shown here for 2D NURBS curves hold for 3D curves, but also for surfaces, as will be used in the models presented later on. A control net is obtained for a surface instead of the control polygon formed by the control points P_i for a curve. An additional knot vector $H = [\eta_1, \eta_2, \dots, \eta_{n+q+1}]$ defines the bivariate NURBS surface of degree p in one direction and degree q in the other. An example is given in Fig. 3

The principle of IGA, as was mentioned before, is to use the NURBS basis functions both for describing the geometry and for approximating the unknowns. For the aerodynamic model the unknowns are the doublet strength, as will be explained in Section 2.2, and for the structural model, the unknowns are the displacements, as will be explained in Section 2.3. The power in this approach lies in the fact that the geometry and its boundary discretisation can be created entirely in CAD software and this geometry can immediately be analysed in the IGA analysis software.

Even though the CAD software provides the exact geometry, the discretisation might not be detailed enough to enable the analysis to provide accurate results. This problem can be easily solved by either knot refinement or degree elevation, or a combination of both [10]. The computational algorithms to perform such operations on NURBS functions are well documented in literature [23]. The knot refinement and degree elevation operations do not affect the geometry itself and can, as a result, be used at any point in a design/analysis process without the need to refer back to the initial CAD geometry.

2.2. Aerodynamic model

The implementation of the aerodynamic model is based on the work by Kim et al. [24]. The potential flow model used for the hydrodynamic analysis of ship propellers in that work is in principle directly applicable to the aerodynamic analysis of aircraft wings. However, to enable the analysis of more complex wing models, multipatch analysis has to be added to the existing work. Furthermore, the Prandtl–Glauert correction is implemented in the model to extend the validity of the model up to high-subsonic Mach numbers. In the following section, a short overview of the aerodynamic model as presented by Kim et al. is given for completeness, together with the extension to multipatch analysis and the implementation of the Prandtl–Glauert correction. The reader is referred to the book by Katz and Plotkin [25] for a comprehensive description of aerodynamic potential flow models and their implementations.

The aerodynamic model is based on the potential flow theory, which assumes incompressible, inviscid and irrotational flow. A flow of this type is described by Laplace's equation. The boundary integral equation resulting from the flow tangency boundary condition is the governing equation for the flow around an wing:

$$\frac{\phi(\mathbf{x}_0)}{2} = - \iint_{S_b} \left(\phi(\mathbf{x}) \frac{\partial G(\mathbf{x}, \mathbf{x}_0)}{\partial \mathbf{n}} + \frac{\partial \phi(\mathbf{x})}{\partial \mathbf{n}} G(\mathbf{x}, \mathbf{x}_0) \right) dS - \iint_{S_w} \left(\Delta \phi(\mathbf{x}) \frac{\partial G(\mathbf{x}, \mathbf{x}_0)}{\partial \mathbf{n}} \right) dS \quad (5)$$

where \mathbf{x} are the boundary coordinates, \mathbf{x}_0 is a specific point on the surface, ϕ is the perturbation velocity potential, $\Delta \phi$ the potential jump in the wake, \mathbf{n} the surface unit normal, S_b and S_w the wing body and wing wake surfaces, respectively, and G the 3-dimensional fundamental solution of Laplace's equation:

$$G = \frac{1}{4\pi r} \quad (6)$$

where $r = |\mathbf{x} - \mathbf{x}_0|$ is the distance between the point of interest and the integration point. From the flow tangency boundary condition, the value for the normal derivative of the velocity potential can be found:

$$\frac{\partial \phi}{\partial \mathbf{n}} = -\mathbf{n} \cdot \mathbf{U}_\infty \quad (7)$$

where \mathbf{U}_∞ is the freestream velocity vector.

The potential jump in the wake is constant in flow direction and is, according to the Kutta condition, equal to the jump in potential at the trailing edge of the wing, so the two surface integrals can be joined together. The isogeometric principle is invoked to discretise the geometry and the perturbation velocity potential as well as its normal derivative, leading to the following discretised boundary integral equation:

$$\frac{\mathbf{R}(\xi_0, \eta_0) \cdot \boldsymbol{\phi}}{2} + \frac{1}{4\pi} \iint_{S_b \cup S_w} \left(\mathbf{R}(\xi, \eta) \frac{\mathbf{n} \cdot \mathbf{r}}{r^3} \right) dS \cdot \boldsymbol{\phi} = -\frac{1}{4\pi} \iint_{S_b} \left(\mathbf{R}(\xi, \eta) \frac{1}{r} \right) dS \cdot \boldsymbol{\sigma} \quad (8)$$

where \mathbf{R} is the matrix with NURBS basis function values, $\boldsymbol{\phi}$ and $\boldsymbol{\sigma}$ are the control points for the perturbation velocity potential and its normal derivative, and \mathbf{r} is the vector, with length r , pointing from the integration point \mathbf{x} to the surface point \mathbf{x}_0 . At this stage the Prandtl–Glauert correction can be introduced. This is done through scaling the geometry in the flow direction by a factor $\beta = \sqrt{1 - M^2}$ in the integrals, where M is the Mach number:

$$\frac{\mathbf{R}(\xi_0, \eta_0) \cdot \boldsymbol{\phi}}{2} + \frac{1}{4\pi} \iint_{S_b \cup S_w} \left(\mathbf{R}(\xi, \eta) \frac{\mathbf{n}(\tilde{\mathbf{x}}) \cdot \mathbf{r}(\tilde{\mathbf{x}}, \tilde{\mathbf{x}}_0)}{r(\tilde{\mathbf{x}}, \tilde{\mathbf{x}}_0)^3} \right) dS \cdot \boldsymbol{\phi} = -\frac{1}{4\pi} \iint_{S_b} \left(\mathbf{R}(\xi, \eta) \frac{1}{r(\tilde{\mathbf{x}}, \tilde{\mathbf{x}}_0)} \right) dS \cdot \boldsymbol{\sigma} \quad (9)$$

where the overhead tilde indicates the coordinates scaled in flow direction by a factor β .

The surface integrals are broken up into the elements that are formed by the non-zero knot spans in the parametric domain. The higher-order discretisation prohibits the use of analytical expressions for the integrals, so Gaussian quadrature is used to evaluate them numerically. The resulting equation is

$$\begin{aligned} \frac{\mathbf{R}(\xi_0, \eta_0) \cdot \boldsymbol{\phi}}{2} + \frac{1}{4\pi} \left[\sum_{i=1}^{n_e} \sum_{g=1}^{n_{gp}} \mathbf{R}(\xi_g, \eta_g) \frac{\mathbf{n}(\xi_g, \eta_g) \cdot \mathbf{r}(\xi_g, \eta_g)}{r(\xi_g, \eta_g)^3} J_1(\xi_g, \eta_g) J_g w_g \right] \cdot \boldsymbol{\phi} \\ = -\frac{1}{4\pi} \left[\sum_{i=1}^{n_e} \sum_{g=1}^{n_{gp}} \mathbf{R}(\xi_g, \eta_g) \frac{1}{r(\xi_g, \eta_g)} J_1(\xi_g, \eta_g) J_g w_g \right] \cdot \boldsymbol{\sigma} \end{aligned} \quad (10)$$

where n_e and n_{gp} are the number of elements and Gaussian quadrature points per element, J_1 the Jacobian for the transformation from the physical to the parametric domain, J_g the Jacobian for the transformation from the parametric to the parent domain in which the Gaussian quadrature points are defined, and w_g the quadrature weights. Eq. (10) can be rewritten in short as

$$\mathbf{h} \cdot \boldsymbol{\phi} = \mathbf{g} \cdot \boldsymbol{\sigma} \quad (11)$$

The integrals are unfortunately not well behaved as the surface point \mathbf{x}_0 approaches the integration point. In the limit, they even become singular since the distance r will go to zero. Special care has to be taken in computing these integrals to be able to obtain accurate results. The singular integrals are computed by splitting the singular element into four triangular elements originating from the singular point to the four corner points. A quadratic transformation is applied to introduce a Jacobian that is zero in the singular point and thus cancels the singularity. The sum of the four triangular integrals will give an accurate result for the integral. For the nearly singular integrals, an adaptive refinement scheme is implemented. Depending on the distance the element under consideration is partitioned into four smaller elements until the characteristic size of the elements is small enough compared to the distance between the element and the surface point \mathbf{x}_0 .

The collocation method is applied to create a system of equations that can be solved for the unknown perturbation velocity potential control points, as in Eq. (12),

$$\mathbf{H} \cdot \boldsymbol{\phi} = \mathbf{G} \cdot \boldsymbol{\sigma} \quad (12)$$

where the rows of \mathbf{H} and \mathbf{G} are the \mathbf{h} and \mathbf{g} taken from Eq. (11). In most of the literature on the application of IGA in boundary element method (BEM) formulations, the Greville abscissae are used as collocation points. In previous work of the authors on 2-dimensional aeroelastic analysis using IGA, these points were also used, so this was also the starting point for the present work. The results when using these collocation points show poor convergence at the trailing edge of the wing. The pressure distribution on the top and bottom side of the wing does not converge at a single point, but instead crosses shortly before the trailing edge point and diverges, as is shown in Fig. 4.

The dynamic Kutta condition, as described in the work of Kim et al. [24], is implemented to reduce this problem. However, to be able to enforce this condition, it is necessary to solve the system of Eq. (12) in a constrained least squares way. The overdetermined system is constructed by placing four collocations points uniformly on every element resulting in more collocation points compared to control points. Together with the dynamic Kutta constraint, it shows better convergence of the pressure distribution at the trailing edge. This is shown in Fig. 4 with the dashed line.

Once the perturbation velocity potential is known, the pressure distribution on the body and the resulting aerodynamic loads can be computed. The loads in the control points are computed by integrating the pressure distribution multiplied by normal vector and the basis function values over the wing surface area. The induced drag is computed using a Trefftz plane analysis [25]. The intersection of the wake with the Trefftz plane is modelled as a NURBS curve to maintain the exact geometrical concept of the isogeometric principle. The singularity subtraction technique (SST) [26] is used to take care of the hypersingular integrals and the Telles transformation [27,28] is applied to the nearly singular integrals.

For a multipatch geometry, the system of Eq. (12) is computed for the entire geometry in one go. At this point, however, measures have to be taken to ensure the proper continuity of the solution. The lowest requirement is to enforce C_0 -continuity, so that overlapping control points of the different patches have the same value for the perturbation velocity potential in the final solution. This is done by introducing a transformation matrix that couples these overlapping control points at the edges of neighbouring patches:

$$\mathbf{H} \cdot \mathbf{T}_{C_0} \cdot \boldsymbol{\phi} = \mathbf{G} \cdot \boldsymbol{\sigma} \quad (13)$$

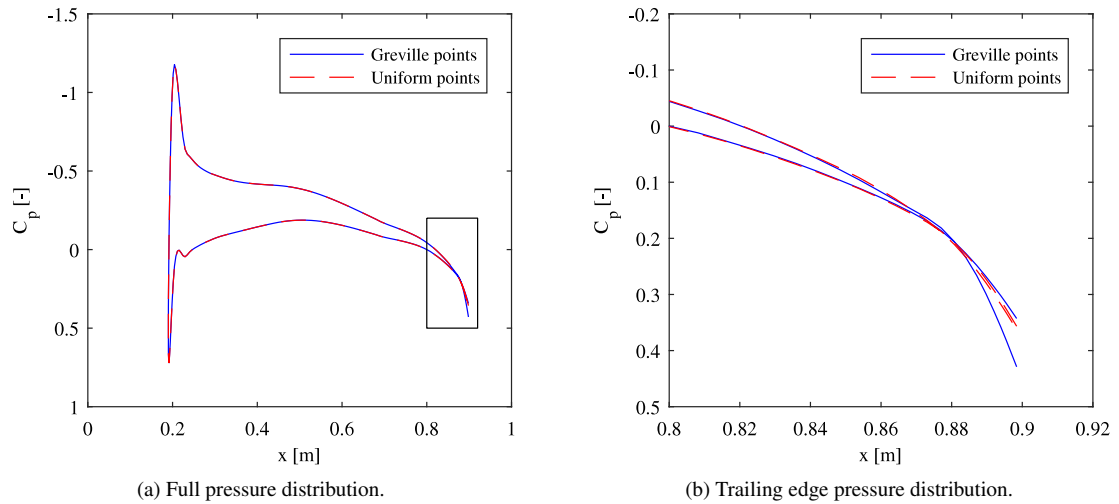


Fig. 4. Pressure distribution of the Onera M6 wing at 33% span using Greville abscissae or uniform points as collocation points.

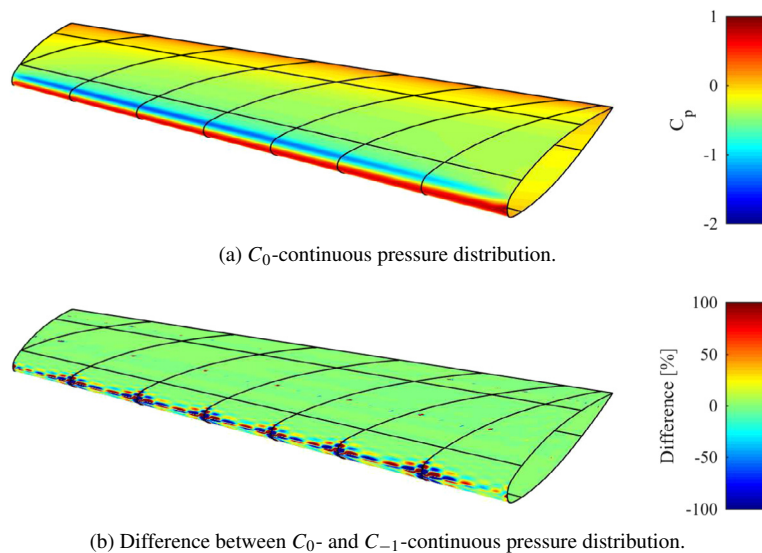


Fig. 5. Comparison of Onera M6 results with C_{-1} and C_0 continuity for a geometry consisting of 39 NURBS patches.

In Fig. 5, the pressure distribution for the Onera M6 wing is shown resulting from the transformation as shown in Eq. (13). The black lines on the surface indicate the boundaries of the 39 NURBS patches forming the wing geometry. The relative difference with the unconstrained pressure distribution is also shown. The extreme values are found at the leading edge around the patch interfaces and exceed 100%, illustrating that enforcing C_0 -continuity is essential for an accurate solution. The large difference in the leading edge zone can be explained by the strong changes in pressure distribution and the pressure distribution crossing zero in this zone. A small deviation in the location where it crosses zero results in large relative differences.

The IGA aerodynamic model is verified by comparing it to the results of the panel code TriPan and the Euler code SUmB [29], as presented in the work of Kennedy and Martins [7]. The pressure distribution of the Onera M6 wing at Mach numbers 0.5 and 0.7 is compared between the three different models at two spanwise locations of the wing. The incoming flow is at an angle of attack of 3.06 degrees. The TriPan results were obtained using 8000 surface panels, the

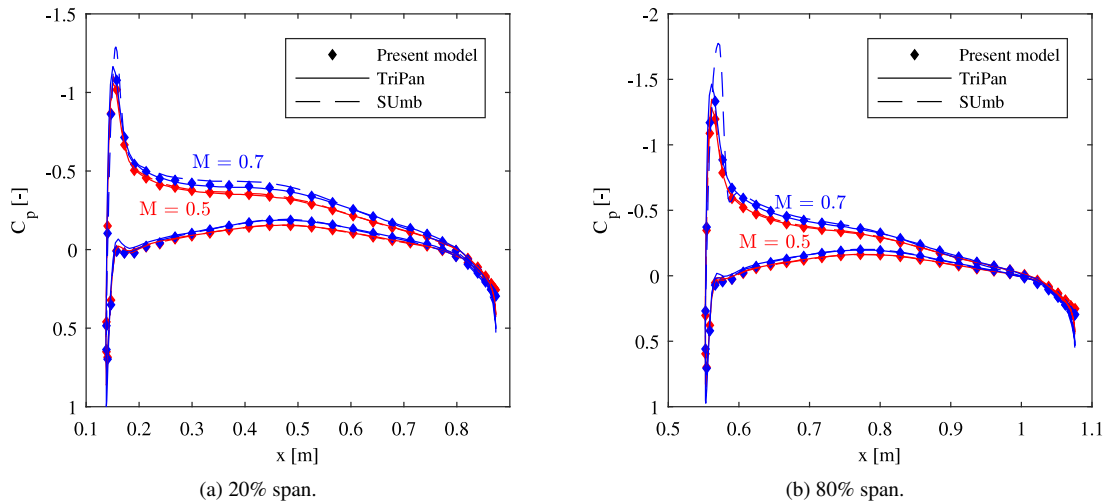


Fig. 6. Comparison of the IGA aerodynamic model with TriPan and Sumb for the Onera M6 wing.

Sumb results with 3.15 million volume cells including 32,768 surface cells, and the present model uses 39 patches with in total 1096 cubic surface elements and 2835 degrees of freedom. The comparison is shown in Fig. 6. For a Mach number of 0.5, the results of the three different models are very similar for both spanwise locations. For Mach 0.7 the results of the present model and TriPan are still close together, but they start to deviate from the results of Sumb especially at the suction peak at the leading edge. This demonstrates that the limit of the potential flow theory including the Prandtl–Glauert correction is indeed somewhere around a Mach number of 0.6 to 0.7. Above this limit, the compressibility effects start to play a significant role in the solution, which the present model is unable to capture.

2.3. Structural model

Considering the shell-like nature of the aerodynamic model, the natural choice for shell elements for the structural representation was made. In general, the wingbox of an aircraft can be seen as a thin-walled structure. Kirchhoff–Love shell elements would be sufficient to represent such a structure. The use of IGA has opened up the doors to applying the Kirchhoff–Love theory due to the increased order of the basis functions [30]. The absence of rotations in the formulation, calls for C_1 continuity of the displacements. In the interior of a NURBS patch, the functions can be of as high a degree as the user requires. Only on the edges of a patch, the continuity decreases to zero, due to the nature of the open knot vectors that are used. Inside the patch, it is thus no problem to use the Kirchhoff–Love theory. For a multipatch model, however, special care has to be taken at the patch interfaces due to the C_0 continuity at these locations [31].

The alternative is using the Reissner–Mindlin shell theory, which includes the rotations and can also be used for thicker shells. The implementation of IGA in a Reissner–Mindlin model was first explored by Benson et al. [32]. The lower complexity of the multipatch implementation of the Reissner–Mindlin theory compared to the Kirchhoff–Love theory has motivated the authors to use this theory for the aeroelastic model presented in this work. A linear shell model based on the work of Dornisch et al. [33,34] is implemented with the addition of the capability to analyse anisotropic structures as well as isotropic ones. The membrane, bending, and shear stiffnesses of the composite materials are parametrised using lamination parameters [35] for future optimisation purposes. In the following section, an overview of the implementation of the anisotropic material in the shell model is given and it is verified.

The stiffness matrix for a Reissner–Mindlin shell made of isotropic material is computed as the volume integral

$$\mathbf{K} = \int_V \mathbf{B}^T \cdot \mathbf{C} \cdot \mathbf{B} dV \quad (14)$$

where the superscript \top indicates the transpose, \mathbf{C} is the material stiffness tensor and \mathbf{B} the matrix describing the relation between the strains and the displacements and rotations. For a derivation of the \mathbf{B} matrix see the work by

Dornisch and Klinkel. [33]. Both matrices can be split into components related to the membrane, bending, and shear deformations:

$$\mathbf{K} = \int_V (\mathbf{B}^m)^\top \cdot \mathbf{C}^m \cdot \mathbf{B}^m dV + \int_V (\mathbf{B}^b)^\top \cdot \mathbf{C}^b \cdot \mathbf{B}^b dV + \int_V (\mathbf{B}^s)^\top \cdot \mathbf{C}^s \cdot \mathbf{B}^s dV \quad (15)$$

The superscripts m , b and s indicate the membrane, bending and shear components, respectively.

For an anisotropic material, it is possible that there is a coupling between the different components of the deformation. For example, an in-plane load may introduce not only in-plane stretching, but also out-of-plane bending deformation. The material stiffness tensor, $\tilde{\mathbf{C}}$, for an anisotropic material can be written as

$$\tilde{\mathbf{C}} = \begin{bmatrix} \mathbf{A} & \mathbf{B} & \mathbf{0} \\ \mathbf{B} & \mathbf{D} & \mathbf{0} \\ \mathbf{0} & \mathbf{0} & \mathbf{A}_s \end{bmatrix} \quad (16)$$

where the \mathbf{A} , \mathbf{B} , \mathbf{D} and \mathbf{A}_s matrices are the extensional stiffness, bending-extensional coupling stiffness, bending stiffness, and transverse shearing stiffness, respectively [36]. Stiffened panels are commonly used for aircraft structures. The stiffeners are not explicitly modelled in the present structural model, but their effect is taken into account by computing a so-called smeared panel stiffness that adds the effect of the stiffeners to all four material stiffness matrices [37]. The global structural stiffness matrix can now be computed as follows:

$$\begin{aligned} \mathbf{K} = & \int_V (\mathbf{B}^m)^\top \cdot \mathbf{A} \cdot \mathbf{B}^m dV + \int_V (\mathbf{B}^m)^\top \cdot \mathbf{B} \cdot \mathbf{B}^b dV + \int_V (\mathbf{B}^b)^\top \cdot \mathbf{B} \cdot \mathbf{B}^m dV \\ & + \int_V (\mathbf{B}^b)^\top \cdot \mathbf{D} \cdot \mathbf{B}^b dV + \int_V (\mathbf{B}^s)^\top \cdot \mathbf{A}_s \cdot \mathbf{B}^s dV \end{aligned} \quad (17)$$

Once the displacements and rotations of the structural nodes have been determined, the strains in the structure can be computed. The \mathbf{B} matrix is stored at a selection of the integration points and by using Eq. (18) the strains in these integration points can be computed:

$$\boldsymbol{\epsilon}^i = \begin{bmatrix} \epsilon_{11}^i \\ \epsilon_{22}^i \\ 2\epsilon_{12}^i \\ \kappa_{11}^i \\ \kappa_{22}^i \\ 2\kappa_{12}^i \\ \gamma_1^i \\ \gamma_2^i \end{bmatrix} = \mathbf{B}^i \cdot \mathbf{u} \quad (18)$$

where $\boldsymbol{\epsilon}$ is a vector with the all the strain components: ϵ_{ij} the membrane strains, κ_{ij} the bending strains, and γ_i the transverse shear strains, and \mathbf{u} is the vector with degrees of freedom. The superscript i indicates the values at integration point i . The strain components are used to compute the engineering strains at the top and bottom of the shells, as the extreme value will be located at either of those. The principal strains at the top and bottom can subsequently be computed by determining the eigenvalues of the infinitesimal strain tensor.

The stresses or strains occurring in the structure can be compared to the material strengths through the available composite strength failure criteria to evaluate whether structural failure occurs or not. However, with a future application in gradient-based structural optimisation in mind, lamination parameters are used for the description of the composite laminates. This means no explicit stacking sequence is available in the analysis and thus the extreme values of the stresses or strains cannot be determined, rendering the strength failure criteria useless in this case. IJsselmuiden et al. [35] derived a failure envelope based on the Tsai–Wu failure criterion which ensures that no failure occurs regardless of the ply angle in the composite laminate. In the present model, the implementation by Khani et al. [38] is used, who reformulated the failure envelope of IJsselmuiden in terms of the principal strains.

The implementation of the anisotropic materials is verified by comparing the results from the present model to those obtained with the commercial finite element analysis (FEA) software Abaqus version 6.13. For the verification, a wingbox for the Onera M6 wing was modelled. It consists of the top and bottom skin panels, a front and rear spar, and eight ribs. All elements have the same thickness of 5 mm. The composite material that is used has the specifications as listed in Table 1. For all elements, a symmetric, unbalanced lay-up of [0/45/45/0] was used. The

Table 1
Material properties (Source: [39]).

UD Carbon/Epoxy (AS4/3501-6)	
E_{11}	147.0 GPa
E_{22}	10.3 GPa
G_{12}	7.0 GPa
G_{23}	3.7 GPa
G_{13}	7.0 GPa
ν_{12}	0.27
ρ	1600 kg/m ³

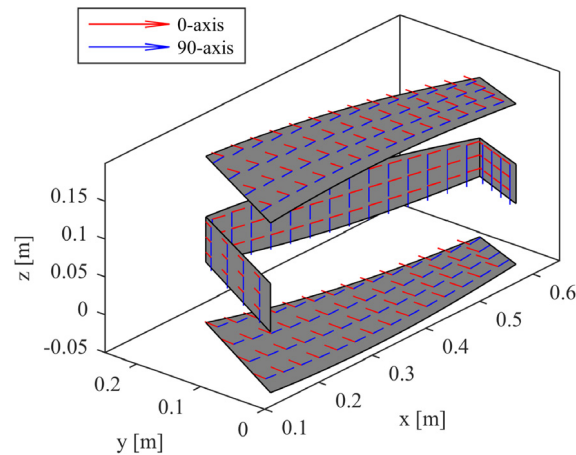


Fig. 7. 0- and 90-degree axes for the composite lay-up definition for the first wingbox bay.

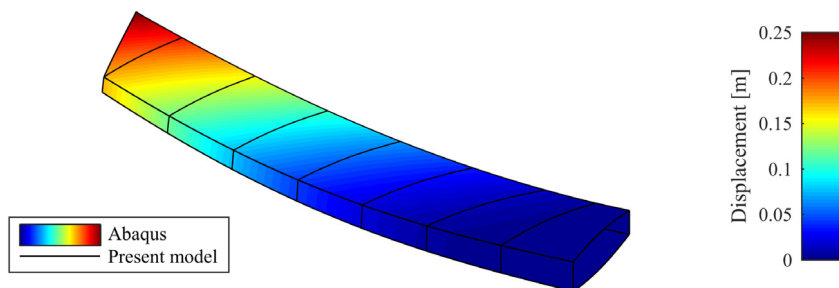


Fig. 8. Structural displacements of the Onera M6 wingbox under a tip load obtained with Abaqus with an overlay of the outline of the deformed wingbox obtained using the present model.

0 and 90 degree directions are as shown in Fig. 7 for the first wingbox bay. The remaining bays follow the same definition. A concentrated load of 50 kN is applied to the tip of the wing at the trailing edge spar, and the wingbox is fully clamped at the root. The Abaqus shell model consists of 12,032 linear S4R elements with a total of 70,800 degrees of freedom, and the IGA model consists of 1412 cubic elements with a total of 12,994 degrees of freedom. The comparison of the displacement field is shown in Fig. 8, where the result of the Abaqus model is shown with on top of that the outline of the deformed geometry obtained using the present model. The maximum displacement of the Abaqus model is 0.2508 m and for the IGA model it is 0.2% lower at 0.2503 m. The comparison of the resulting strain field is shown in Fig. 9. The minimum principal strain of the top outside surface is shown for the two models, which again show a good similarity. The strain values of the present model are computed in the integration points which are in the interior of the elements. Within each patch, the strain values are interpolated to be able to plot the strain field. The values are not, however, extrapolated to the edge of the patches, explaining the white lines visible in

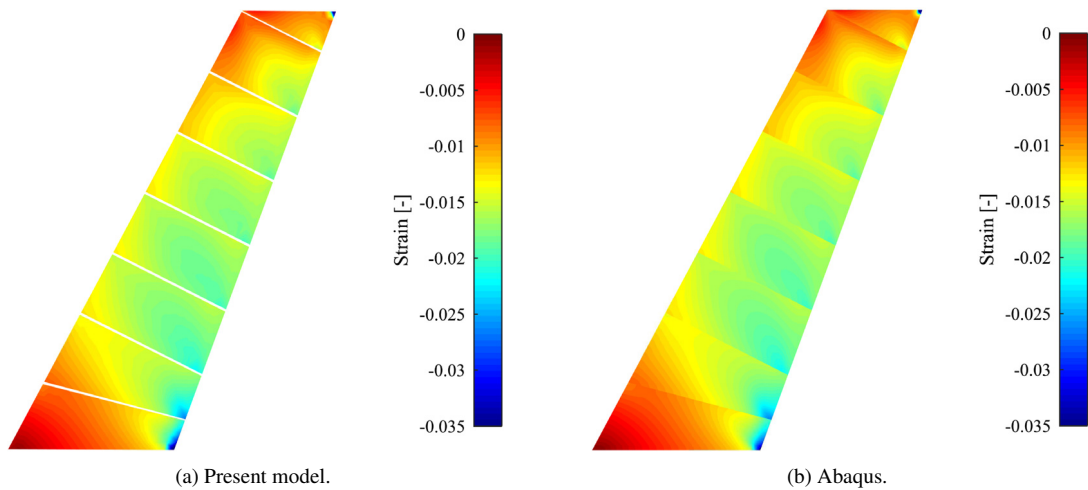


Fig. 9. Minimum principal strain in the top surface of the Onera M6 wingbox obtained using the present model and Abaqus.

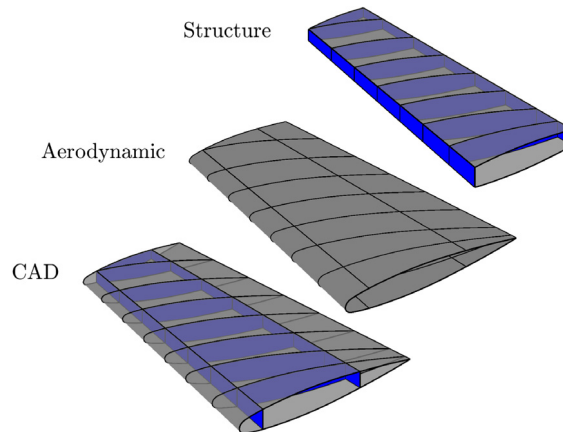


Fig. 10. The CAD, aerodynamic and structural geometries.

between the patches. The strains in the rest of the structure, as well as the maximum principal strains, show similar likeness between the models.

2.4. Aeroelastic coupling

Coupling the previously described aerodynamic and structural models will enable the simulation of the static aeroelastic behaviour of aircraft wings. In previous work of the authors on two-dimensional isogeometric aeroelastic analysis, it was concluded that the non-interpolatory nature of the NURBS geometry introduces some difficulties in the coupling process.[21] In that work, the gradient matrices that contain the gradients of the control points of the aerodynamic and structural mesh with respect to the control points of the coarse CAD mesh were used to couple the two disciplines. The fact that all three geometries were largely the same made it relatively easy to use this procedure.

In the present work, the CAD model contains all geometrical features, but the aerodynamic model consists of only the outer skin of the wing model, and the structural model consists of only the wingbox, as is shown in Fig. 10.

This complicates the coupling using the gradient matrices, as this requires the extrapolation of the displacements of the wingbox to the leading and trailing edge sections of the wing before transferring the displacements to the aerodynamic mesh. Considering the non-interpolatory nature of the NURBS and that the aeroelastic model is meant

to be used in fully free shape optimisation, this is not a trivial task. Furthermore, the structural displacements are mapped onto the coarser CAD mesh before being mapped onto the aerodynamic mesh in the aforementioned method. As a result, the displacement field of the aerodynamic mesh can only be as complex as the CAD mesh allows it to be. This thus increases the requirements of the CAD mesh in terms of the number of control points and degree of the basis functions. These two problems made the gradient matrix method unappealing for the present work, and a different approach was sought for this three-dimensional coupling problem.

Coupling the control points directly is difficult due to them not lying on the surface and thus not being interpolatory. To circumvent this problem, the NURBS geometry of the aerodynamic model is evaluated in the Greville abscissae and the structural model in a user defined selection of points. The Greville abscissae can be also be used for the structural points, but a reduced set of points will lower the computational cost of the RBF interpolation [40] without compromising the accuracy. The user could, for example, chose to use a set of n by n equally spaced points per patch instead.

The Greville abscissae in the parametric space of the NURBS patches can be computed as follows:

$$\bar{\xi}_i = \frac{\xi_{i+1} + \xi_{i+2} + \dots + \xi_{i+p}}{p}, \quad i = 1, 2, \dots, n \quad (19)$$

The computed surface points can subsequently be coupled to each other through RBF interpolation. The basis function values at the surface points are stored in separate matrices, \mathbf{R}_a and \mathbf{R}_s , and are used to retrieve the coupling matrix $\tilde{\mathbf{H}}$ that couples the structural (subscript s) and aerodynamic (subscript a) control points:

$$\mathbf{R}_a \cdot \mathbf{P}_a = \mathbf{H} \cdot \mathbf{R}_s \cdot \mathbf{P}_s \quad (20)$$

$$\mathbf{P}_a = \tilde{\mathbf{H}} \cdot \mathbf{P}_s \quad (21)$$

$$\tilde{\mathbf{H}} = \mathbf{R}_a^{-1} \cdot \mathbf{H} \cdot \mathbf{R}_s \quad (22)$$

where \mathbf{P}_a and \mathbf{P}_s are the aerodynamic and structural control points, and \mathbf{H} the coupling matrix for the surface points $\mathbf{x}_a = \mathbf{R}_a \cdot \mathbf{P}_a$ and $\mathbf{x}_s = \mathbf{R}_s \cdot \mathbf{P}_s$. Using the Greville abscissae for the aerodynamic surface points, results in a invertible square matrix \mathbf{R}_a with a good coverage of the complete model. The transformation matrix can now be used to couple the translational structural degrees of freedom to the translations of the aerodynamic control points.

The aerodynamic and structural geometries are split up into two groups for the coupling. The leading and trailing edges of the aerodynamic geometry are coupled to the spars and ribs only. The remaining aerodynamic panels are coupled to the upper and lower skin panels of the wingbox. This is done to avoid problems with local peak loads on the skin of the wingbox. Direct coupling of the full aerodynamic model to the full structural model would result in considerable out-of-plane forces on the wingbox skin panels. The panels would deform excessively, as they are not designed to carry such a load. By coupling the leading and trailing edges to the spars and ribs only, a more realistic load transfer is obtained and the skin panels carry only the load for which they were designed. The two coupling matrices are in the end assembled into a single matrix.

Once the coupling matrix is determined, the structural displacements can be transferred to the aerodynamic mesh using Eq. (23):

$$\mathbf{u}^a = \tilde{\mathbf{H}} \cdot \mathbf{u}^s \quad (23)$$

where the superscripts a and s indicate whether the variable is defined on the aerodynamic or the structural mesh, respectively. With the transpose of the coupling matrix, the aerodynamic loads can be transferred to the structural mesh:

$$\mathbf{f}_a^s = \tilde{\mathbf{H}}^T \cdot \mathbf{f}_a^a \quad (24)$$

The accuracy of the coupling method is verified through graphical inspection of the aerodynamic and structural meshes and by numerically inspecting the force transfer and resultant forces and moments. In Fig. 11, both the aerodynamic and structural geometries under aeroelastic deformation are shown on top of each other. The interpolation and transfer of the structural displacements to the aerodynamic mesh give accurate and smooth aerodynamic displacements. The force and moment resultants on both meshes are identical, as is shown in Table 2.

The coupling matrix $\tilde{\mathbf{H}}$ can now be used to set up the governing equations for the aeroelastic system comprised of the IGA aerodynamic and structural models described before. The first equation is the balance of internal and external loads:

$$\mathbf{f}_{in} - \mathbf{f}_{ext} = \mathbf{f}_s - \mathbf{f}_a - \mathbf{f}_e = \mathbf{0} \quad (25)$$

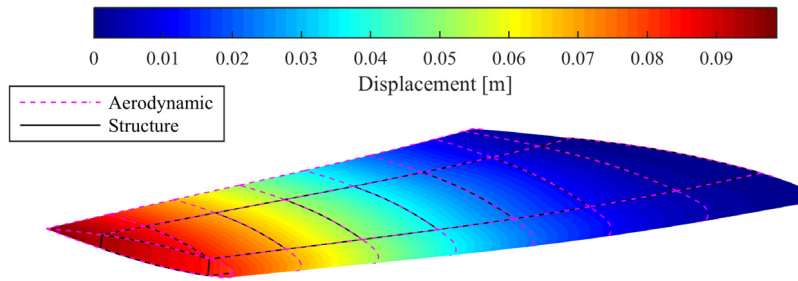


Fig. 11. The deformed aerodynamic and structural models on top of each other.

Table 2

Aerodynamic and structural force and moment resultants.

	F_x [N]	F_y [N]	F_z [N]	M_x [Nm]	M_y [Nm]	M_z [Nm]
Aerodynamic	-159.93	120.86	2418.2	1269.1	-1126.2	162.99
Structure	-159.93	120.86	2418.2	1269.1	-1126.2	162.99

where \mathbf{f}_s are the internal structural loads, \mathbf{f}_a the aerodynamic loads, and \mathbf{f}_e any remaining external loads, such as for instance gravitational loads, fuel loads or engine thrust. The equation is linearised using a Taylor series expansion to end up at the monolithic governing linear system, which is solved on the structural mesh:

$$\begin{aligned}
 (\mathbf{K}_s^s - \mathbf{K}_a^s - \mathbf{K}_e^s) \cdot \mathbf{u}^s &= \mathbf{f}_{a,0}^s + \mathbf{f}_{e,0}^s \\
 (\mathbf{K}_s^s - \tilde{\mathbf{H}}^T \cdot \mathbf{K}_a^a \cdot \tilde{\mathbf{H}} - \mathbf{K}_e^s) \cdot \mathbf{u}^s &= \tilde{\mathbf{H}} \cdot \mathbf{f}_{a,0}^a + \mathbf{f}_{e,0}^s \\
 \mathbf{J} \cdot \mathbf{u}^s &= \tilde{\mathbf{H}} \cdot \mathbf{f}_{a,0}^a + \mathbf{f}_{e,0}^s = \mathbf{R}_0
 \end{aligned} \tag{26}$$

where \mathbf{K}_s , \mathbf{K}_a and \mathbf{K}_e , are the gradients of the forces with respect to the displacement and thus the structural, aerodynamic and external force stiffness matrices. The subscript 0 refers to the forces as computed for the undeformed initial configuration. The structural stiffness matrix is directly available from the structural model. The aerodynamic and external stiffness matrices are the gradients of the corresponding forces with respect to the structural degrees of freedom and are computed analytically. This monolithic system can be solved in one go to find the aeroelastic solution, whereas a typical staggered approach requires an iterative process to end up in the point of equilibrium. The monolithic approach is thus computationally more efficient and stable.

With Eq. (26) the aeroelastic deformation can be determined at a constant angle of attack of the wing. To be able to perform aeroelastic analysis in a trimmed configuration, an additional equilibrium equation is required. The trim equation makes sure that the lift is equal to the weight:

$$L - W = 0 \tag{27}$$

The same linearisation procedure is followed with the unknown now being the angle of attack α of the wing. Combining the two governing equations results in the complete aeroelastic system:

$$\begin{bmatrix} \mathbf{J} & -\left(\frac{\partial \mathbf{f}_a^s}{\partial \alpha} + \frac{\partial \mathbf{f}_e^s}{\partial \alpha}\right) \\ \frac{\partial L}{\partial \mathbf{u}} & \frac{\partial L}{\partial \alpha} \end{bmatrix} \cdot \begin{bmatrix} \mathbf{u}^s \\ \Delta \alpha \end{bmatrix} = \begin{bmatrix} \mathbf{R}_0 \\ W - L_0 \end{bmatrix} \tag{28}$$

Once the aeroelastic deformations and the trimmed angle of attack are determined, the strains can be computed as was already described in Section 2.3, as well as the buckling and boundary layer behaviour as is described in the next section.

The aeroelastic analysis is verified by comparing results for the Onera M6 wing with results obtained using SOL 144 in MSC.Nastran version 2014.1. The Onera M6 was originally not designed with an aeroelastic application in mind. The wing is relatively short and stiff and thus shows little aeroelastic coupling. The skin panels can be made thinner to promote aeroelastic deformations. This, however, will at some point result in significant deformations of

Table 3

Aeroelastic results for Onera M6 wing at an equal angle of attack for the present and MSC.Nastran models.

	Present model	MSC.Nastran	Difference
Angle of attack [deg]	3	3	0.00%
Rigid lift [N]	1387.7	1313.6	5.64%
Elastic lift [N]	899.6	856.8	5.00%
Tip displacement [m]	0.1494	0.1403	6.49%

Table 4

Aeroelastic results for Onera M6 wing at an equal rigid lift for the present and MSC.Nastran models.

	Present model	MSC.Nastran	Difference
Angle of attack [deg]	3	3.16	−5.06%
Rigid lift [N]	1387.7	1387.9	−0.01%
Elastic lift [N]	899.6	905.2	−0.62%
Tip displacement [m]	0.1494	0.1483	0.74%

the airfoil in between the ribs due to the aerodynamic pressures acting on the skin. In the present verification case, the material stiffness properties are lowered instead of lowering the skin thickness to ensure sufficient bending stiffness and consequently avoid too large airfoil deformations.

The isotropic material that is used for the verification has a Young's modulus of 147 MPa and a Poisson's ratio of 0.27. A thickness of 10 mm is used for all skin, spar and rib panels. The Mach number is 0.7, the altitude 35,000 ft, and the angle of attack 3 degrees. The wingbox is modelled in MSC.Nastran using CQUAD4 elements and the aeroelastic coupling is created using the SPLINE4 card with all aerodynamic and all structural nodes included.

The results of the two models are shown in Table 3. The tip displacement of the present model is about 6.5% higher compared to that of the MSC.Nastran model. This can be explained by the different aerodynamic models that are used. The MSC.Nastran model uses the doublet lattice model, in which the wing thickness is not modelled and thus not taken into account. This results in a lower aerodynamic lift as is also shown in Table 3.

To compensate for the lower lift the angle of attack of the MSC.Nastran model is slightly increased, such that the rigid lift of the two models are approximately equal. The results of this updated simulation are shown in Table 4 and show that the displacement results are now within 1% of each other.

2.5. Post-processing

The results of the aeroelastic analysis are used to determine whether or not any buckling is occurring in the structure and to compute the viscous drag in the deformed trimmed configuration in a post-processing step. First, the buckling implementation is described.

Typically, the wingbox inside aircraft wings consists of the top and bottom stiffened skin panels, two or more spars, and a number of ribs. As explained in Section 2.3, in the present work, the stiffeners on the skin panels are not explicitly modelled. These stiffeners do have a large influence on the buckling behaviour of the wingbox, so for the buckling analysis, the user can add stiffeners for buckling purposes only. To reduce the computational cost of the complete model, it is also possible to reduce the number of modelled ribs and add ribs for the buckling analysis only.

The curvatures in the wingbox structure are typically low, so they can be modelled as flat plates instead of curved shells to reduce the computational cost. This will result in a conservative approximation of the buckling load. The IGA plate buckling model follows the derivation of Shojaee et al. [41], but with a more general load definition instead of expressing the in-plane loads as a factor times one load value. The Kirchhoff–Love plate model only has the out-of-plane deformations as unknowns, since the buckling panels are modelled as simply supported plates. This choice is made to ensure a conservative approximation of the buckling load by assuming the bending loads of any individual plate cannot be transferred to the surrounding structure.

The eigenvalue problem that has to be solved to find the buckling load is as follows:

$$(\mathbf{K} - \lambda_i \mathbf{K}_g) \cdot \mathbf{w}_i = 0 \quad (29)$$

where \mathbf{K} is the global stiffness matrix, \mathbf{K}_g the geometric stiffness matrix, and λ_i and \mathbf{w}_i the i th buckling load and mode shape, respectively. The global stiffness matrix is obtained in a similar way as was done for the Reissner–Mindlin

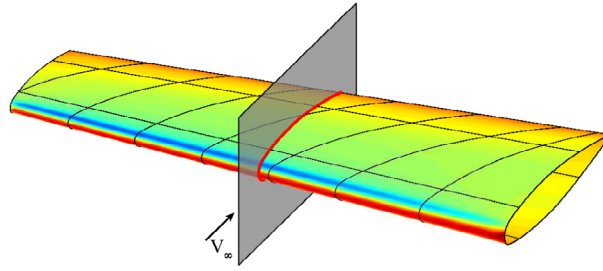


Fig. 12. Onera M6 geometry with cutting plane and intersection curve.

shell model, except that the strain–displacement relation is now different and only the \mathbf{D} material matrix is used for the out-of-plane displacement. The geometric stiffness matrix is obtained as a function of the internal in-plane loads:

$$\mathbf{K}_g^{ij} = \int_V \tilde{\mathbf{B}}_i^\top \cdot \tilde{\mathbf{n}} \cdot \tilde{\mathbf{B}}_j dV \quad (30)$$

where $\tilde{\mathbf{n}}$ is the integral through the plate thickness of the in-plane internal stresses and $\tilde{\mathbf{B}}_i$ a vector with shape function derivatives in integration point i :

$$\tilde{\mathbf{B}}_i = \begin{bmatrix} \frac{\partial R_i}{\partial x} \\ \frac{\partial R_i}{\partial y} \end{bmatrix} \quad (31)$$

The geometry of the buckling plates is derived from the structural model and the user-supplied information on stiffener and additional rib locations. A projection method is used to go from a curved panel bounded by stiffeners and ribs to a flat buckling plate. The in-plane loads in the integration points of the buckling plate are determined by projecting these points back onto the curved panel and evaluating the loads in those points while taking into account the transformation in coordinate systems.

The other post-processing step is computing the viscous drag. The inviscid potential flow model as described in Section 2.2 can only provide the induced drag. A higher fidelity model is necessary to obtain the viscous drag component. In the present work, a quasi-3D boundary layer model is implemented based on the previous work from the authors on 2D aeroelastic analysis [21]. Contrary to other literature on this subject, where for the drag analysis separate 2D aerodynamic analyses of the wing sections are done [42–44], in the present model the 3D flow field computed with the 3D aerodynamic model is directly used as input for the boundary layer analysis. Several sections of the flow field are extracted to obtain the velocity field around the local airfoils. This data is then used in the 2D boundary layer model to approximate the viscous drag.

The 2D sections of the geometry and flow field are determined by finding the intersection between the NURBS geometry and a vertical plane in flow direction at a number of spanwise locations, as is illustrated in Fig. 12 for a single cutting plane. The intersection is determined by the marching algorithm as described by Hu et al. [45]. Once the local airfoil and tangential velocity field are determined, the boundary layer model, consisting of Thwaites' method for laminar flow, Head's method for turbulent flow, and Michel's method for the transition, is used to compute the growth of the boundary layer from the stagnation point to the trailing edge. The Squire–Young formula is used to predict the viscous drag resulting from the boundary layer. For an extensive description of the methods involved in this model and their implementation, see the book by Moran [46].

The sectional drag coefficients are used to approximate the drag of the complete wing through a piecewise constant integral over the surface, divided by the planform area:

$$C_{D_v} = \frac{2}{S} \int_0^{b/2} C_{d_v} c dy \quad (32)$$

where C_{D_v} and C_{d_v} are the 3D and sectional viscous drag coefficients, S the wing planform area, b the span, and c the chord length.

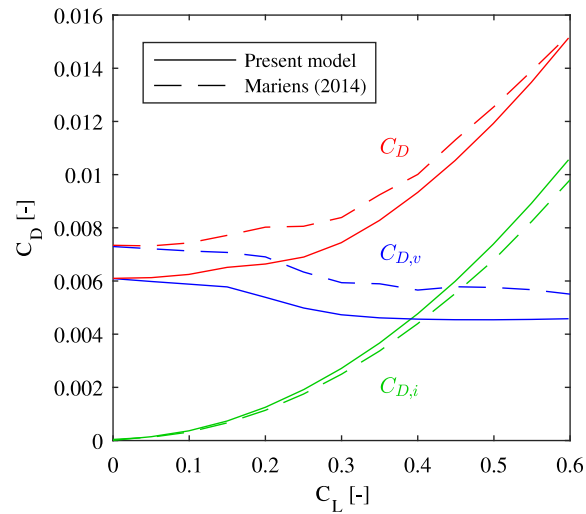


Fig. 13. Comparison of drag components versus lift for the Fokker 50 wing for the present model and results from Mariens et al. [42].

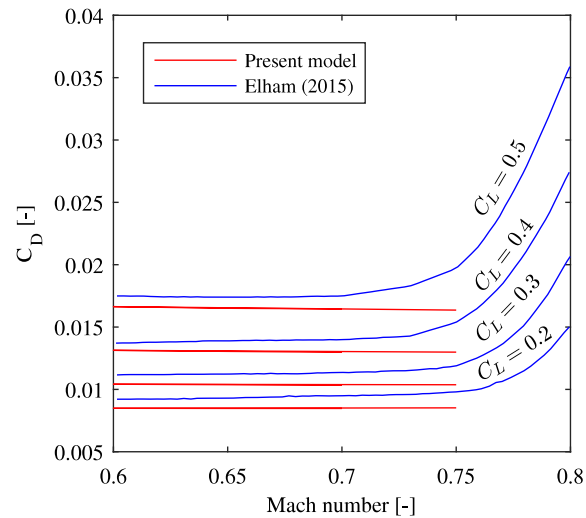


Fig. 14. Comparison of total drag versus Mach number for the Fokker 100 wing for the present model and results from Elham [43].

The drag approximation method is verified by comparing the drag of the Fokker 50 and Fokker 100 wings to reference data taken from the work of Mariens et al. [42] and Elham [43]. In these references, their quasi-3D aerodynamic model is compared to results obtained using the higher-fidelity code MATRICS-V [47], which is based on full potential theory with a 3D integral boundary layer model. This data is used to verify the boundary layer model presented here.

In Fig. 13, the total drag and its induced and viscous components of the Fokker 50 wing are compared at different lift coefficients. The present model shows a slightly steeper increase of the induced drag and an underestimation of the viscous drag. The movement of the transition lines on the top and bottom of the wing with increasing lift is accurately captured as can be seen by the similarity in the trend of the viscous drag component with respect to the reference data. For the Fokker 100 wing, an underestimation of the drag is observed as well, as is shown in Fig. 14. The limitation of the potential flow model is also clearly seen in these results, as the increasing wave drag at higher Mach numbers is not taken into account, resulting in a larger deviation with respect to the reference data for increasing Mach number.

The accuracy of the viscous drag estimation is suitable considering the goal and application of the present framework. For the future optimisation purposes, the trends of the viscous drag are more important than the actual

Table 5
Material strengths (Source: [39]).

UD Carbon/Epoxy (AS4/3501-6)	
X_t	948.5 MPa ^a
X_c	717.6 MPa ^a
Y_t	23.7 MPa ^a
Y_c	94.8 MPa ^a
S	31.6 MPa ^a

^a Including knockdown factors for environmental, barely visible impact damage, and material scatter effects. [50].

values, especially when taking into account the complexity of computing viscous drag for complex geometries. It does, however, need to be taken into account that it is not directly possible to use the drag value in a combined aerostructural objective, as this would result in an unrealistic balance between the two disciplines.

3. Results

To demonstrate the unified isogeometric aeroelastic framework as described in the previous sections, the undeflected Common Research Model (uCRM) wing is analysed, and the results are presented in this section. This model is derived from the well-known Common Research Model (CRM) and provides the jig shape that results in the actual CRM outer mold shape in 1g cruise condition, as explained by Kenway et al. [48]. This wing model is thus ideally suited for aeroelastic analysis as it provides the geometry in an unloaded condition. The span of the uCRM measures 58.9 m, the leading edge sweep is 37 degrees, and the wing surface area is 383.7 m². The mass of the aircraft excluding the wing and all external masses connected to the wing is 130 202 kg. [49]

3.1. Model description

The wingbox presented in the work of Kenway et al. consists of two spars and 48 ribs. In the present work, the layout of the ribs is modified slightly to avoid the rib–rib intersections at the transition from the centre wingbox to the actual wing structure. In the present model, a gradual change in the angle of the ribs is implemented instead of the discrete jump, resulting in one less rib in total. This is done because of the requirement in the current framework to have a patch boundary at every connection between skin and internal structure. The rib–rib intersections would require an even higher number of patches, which would increase the computational cost considerably. The CAD model as used in the present work is shown in Fig. 15.

The structural design of the wingbox used in the present work is based on engineering judgement and is by no means optimised for structural or aerodynamic performance. The goal is to analyse a feasible and realistic design to show the capabilities of the aeroelastic framework. The structural model as described in the remainder of this section results in a wingbox with a mass of around 16,000 kg without taking into account stiffener mass. Comparing this value to values found in literature and taking into account it is not optimised, it can be considered to be a realistic value [3,49].

The stiffener and rib distribution used for the buckling analysis is shown in Fig. 16. A stiffener pitch of around 25 to 30 cm is used. The stiffeners are placed along the parametric coordinates of the NURBS patches. The ribs are stiffened in both horizontal and vertical directions. The spars are only stiffened in the vertical direction.

The composite material for the skin, spars and ribs is the same as was used in the structural verification and is given in Table 1. Additionally, the material strengths, given in Table 5, are used for evaluating the failure criterion.

The directional stiffness distribution on the top skin resulting from the lamination parameters is shown in Fig. 17, where the rosettes indicate the membrane and bending modulus of elasticity as a function of the polar angle θ as computed using Eqs. (33) and (34), respectively, [51]

$$E_{m11}(\theta) = \frac{1}{A_{11}^{-1}(\theta)} \quad (33)$$

$$E_{b11}(\theta) = \frac{1}{D_{11}^{-1}(\theta)} \quad (34)$$

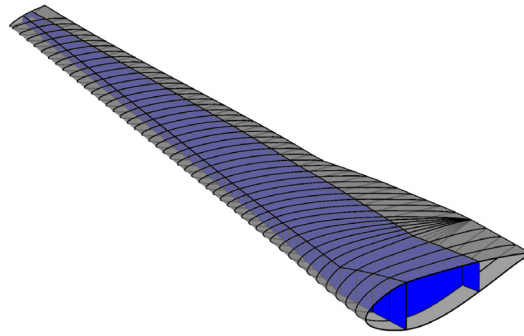


Fig. 15. Complete CAD model of the uCRM wing with wingbox and aerodynamic surfaces.

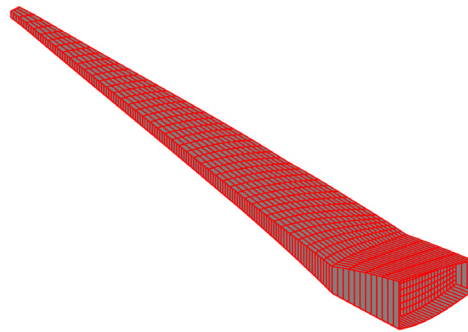


Fig. 16. uCRM wingbox with stiffener and rib layout for the buckling analysis.

where

$$\mathbf{A}^{-1}(\theta) = \mathbf{T}^T \cdot \mathbf{A}^{-1} \cdot \mathbf{T} \tag{35}$$

$$\mathbf{D}^{-1}(\theta) = \mathbf{T}^T \cdot \mathbf{D}^{-1} \cdot \mathbf{T} \tag{36}$$

and

$$\mathbf{T} = \begin{bmatrix} \cos^2(\theta) & \sin^2(\theta) & 2 \cos(\theta) \sin(\theta) \\ \sin^2(\theta) & \cos^2(\theta) & -2 \cos(\theta) \sin(\theta) \\ -\cos(\theta) \sin(\theta) & \cos(\theta) \sin(\theta) & \cos^2(\theta) - \sin^2(\theta) \end{bmatrix} \tag{37}$$

The stiffness is aligned with the swept leading edge and is the same for all the panels shown in Fig. 17. The bottom skin has the same stiffness characteristics. The ribs and spars are composed of a quasi-isotropic laminate. The thickness of the wingbox panels is shown in Fig. 18. The bottom skin experiences significantly higher strains compared to the top skin, as will be demonstrated later in this section, and is thus thicker. This is consistent with designs from other literature. [3,52]

The external masses and loads acting on the wing, such as landing gear, fuel and engine, are taken from the work of Werter [53] and are introduced as either concentrated or distributed loads. An engine thrust of 60 kN is used based on the assumption of a lift-over-drag ratio of the aircraft of around 20.

Three load cases are analysed to demonstrate the computational framework. Firstly, the clamped wing at 1.0 g cruise condition is analysed for aeroelastic deformation and drag. Secondly and thirdly, a 2.5 g symmetric pull-up and a -1.0 g symmetric push-down condition are analysed for structural deformations, strength, and buckling. In general, a cruise Mach number of 0.85 is used for the CRM. In the present model, however, this would be outside of the region of applicability of the potential flow model. For the present work, a cruise Mach number of 0.7 is used instead. This reduced speed will lead to a lower lift generated by the wing, which would result in a relatively high angle of attack in the cruise condition. To compensate for this lower speed, the cruise altitude is lowered from the normally used

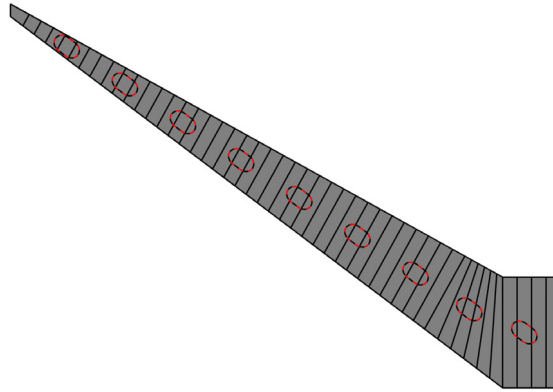


Fig. 17. Stiffness distribution in top skin panels of the uCRM model.

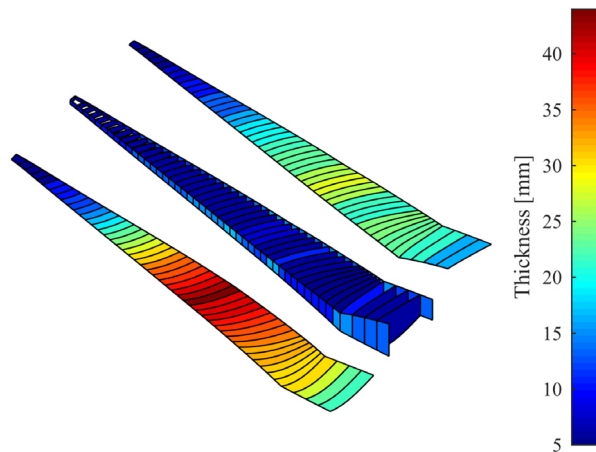


Fig. 18. Thickness distribution of the uCRM model.

37,000 ft to 30,000 ft. The pull-up and push-down load cases are performed at the same Mach number but at a lower altitude of 10,000 ft. All simulations are performed with a full fuel load.

3.2. Cruise load case

In the 1.0 g flight condition, the maximum tip displacement is 1.64 m. It occurs at the trailing edge tip due to the wash-out effect caused by the swept geometry. In the work of Kenway and Martins [3], a tip displacement of approximately 1.52 m was found, which indicates that the structural design used in the present work is indeed reasonable. The complete deformation field is shown in Fig. 19, together with the deformation fields of the other load cases.

To be able to estimate the drag of the wing at cruise condition, the aerodynamic analysis is performed on the deformed geometry, as was explained before. The pressure distribution in the deformed configuration is shown in Fig. 20. The angle of attack for the trimmed cruise flight is 3.5 degrees resulting in a lift coefficient of 0.78. The lift-induced drag is equal to 0.032.

For the quasi-3D viscous drag prediction, the part of the wing that represents the centre wingbox is ignored and only the part that is actually in the airflow is taken into account. This part is sliced at ten uniformly distributed locations to determine the local 2D flow field. The boundary layer model results show that the upper side of the wing is almost fully turbulent, with the transition from the laminar zone in the first 10% of the chord. The lower side of the wing has

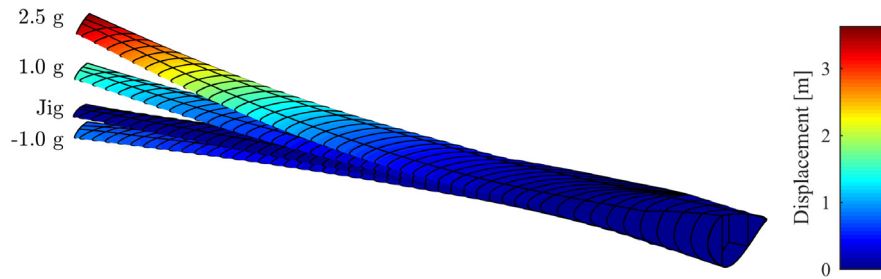


Fig. 19. Initial and deformed geometry of the uCRM wing under 1.0 g cruise, 2.5 g pull-up, and -1.0 g push-down loading conditions.

a larger laminar zone and changes to turbulent at around 55% of the chord. The transition lines for the top and bottom side are shown in Fig. 21. The resulting viscous drag coefficient is equal to 0.015, bringing the total drag coefficient to 0.047.

3.3. Pull-up load case

The maximum tip displacement for the 2.5 g load case is 3.63 m at the trailing edge tip. This is a relatively large displacement compared to the span of the wing, so caution has to be taken with respect to the use of the linear structural model in this case. In future work, it would be advisable to switch to a non-linear structural solver. The full displacement is again shown in Fig. 19.

The values of the Tsai–Wu failure criterion in the wingbox are shown in Fig. 22(a), where a value below 1 means that there is no failure. It can be seen that the bottom wing is most critical, which explains the required higher skin thickness on this side, as was already shown in Fig. 18. At the intersections of the spars and ribs, local peaks in the strain can be observed. This is caused by the coupling of the leading and trailing edges to the structural members, as was explained before. The loads from these aerodynamic surfaces are fully transferred to the spars and ribs connections, resulting in load concentrations at these points. The same effect can be seen at the points where the engine and landing gear loads are introduced in the structure. The fuel loads are distributed over the spars, so the effect is smaller there. In most of these peak locations, the Tsai–Wu criterion is higher than 1.0 meaning the current wing design would fail in these locations. A more accurate model of the load introduction and local structural reinforcement would overcome this issue, but this falls outside the scope of the demonstration of the present model.

The buckling criterion for all the buckling panels in the wingbox is shown in Fig. 22(b), where again a value below 1 means no buckling. The figure shows that only in the top skin towards the wing tip buckling plays a significant role. In the rest of the wingbox, the strength criterion is more important for the present model.

3.4. Push-down load case

The -1.0 g load case induces a displacement field in the opposite direction as the other two load cases, as is shown in Fig. 19. This results in a downward displacement of -0.78 m at the leading edge tip. From the strength and buckling results in Figs. 23(a) and 23(b), it is clear that this load case is less critical than the 2.5 g load case for the present design. The strain concentrations due to the leading and trailing edge are more clearly visible now, due to the lower level of strain in the rest of the wingbox.

4. Conclusions

A computational framework was presented for the aeroelastic analysis of aircraft wings using the isogeometric analysis concept to create a consistent approach for the geometry throughout the analysis. A multi-patch isogeometric aerodynamic potential flow model of the full wing is coupled to a multi-patch isogeometric structural model of the wingbox through a RBF interpolation routine. The structural model supports anisotropic materials, and stiffened panels can be represented through a smeared stiffness approach. In both disciplines, the relevant parts of the same CAD model are used to ensure a consistent geometry throughout the analysis. The resulting aeroelastic deformations

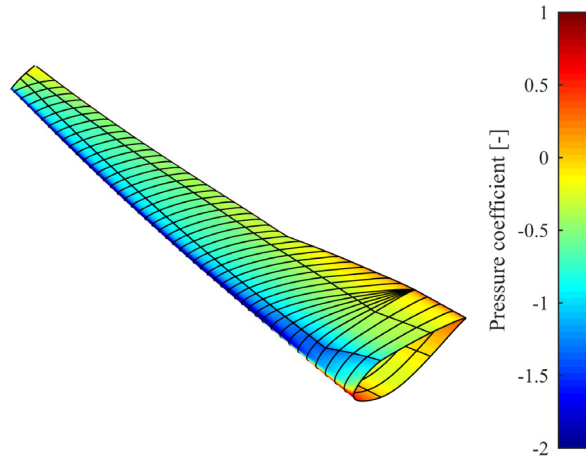


Fig. 20. Pressure distribution of the uCRM wing at 1.0 g cruise condition.

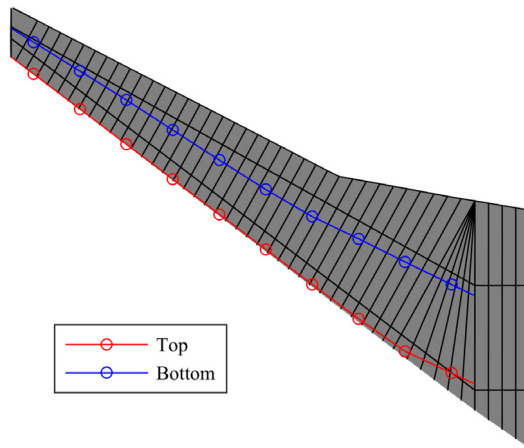
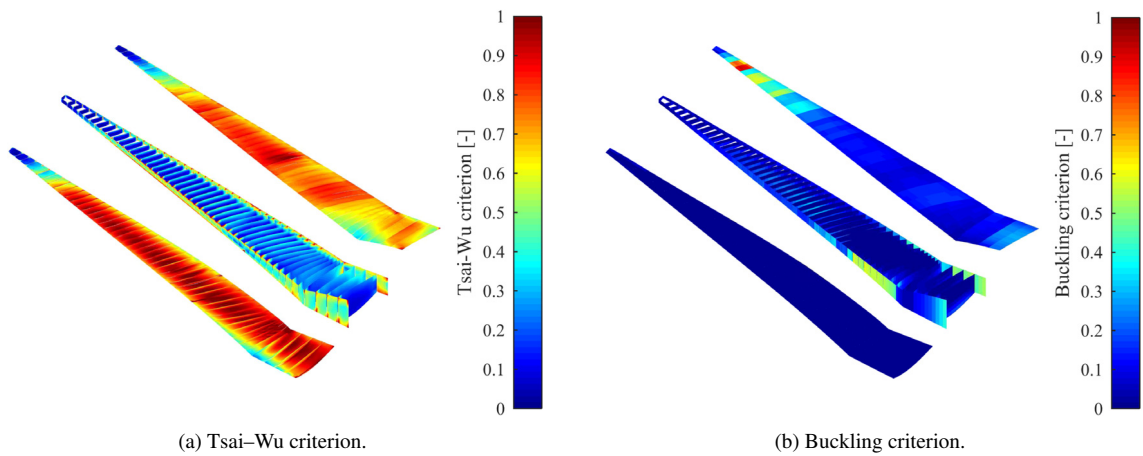


Fig. 21. Transition lines on the top and bottom side of the uCRM wing at 1.0 g cruise condition.



(a) Tsai–Wu criterion.

(b) Buckling criterion.

Fig. 22. Structural results for the uCRM wing under a 2.5 g symmetric pull-up load.

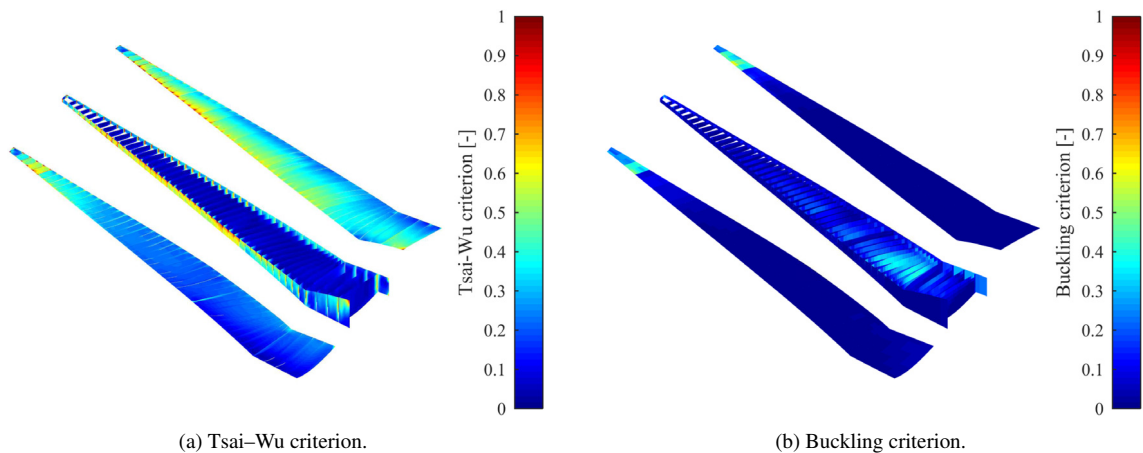


Fig. 23. Structural results for the uCRM wing under a -1.0 g symmetric push-down load.

are used to compute strains and evaluate the strength criterion. The local buckling behaviour is investigated with an isogeometric plate buckling model, and the viscous drag is estimated using a quasi-3D boundary layer model that uses the 3D flow field from the potential flow model as input.

The separate parts of the framework were verified against reference solutions. The aerodynamic verification demonstrated that using the Greville abscissae as collocation points results in unfavourable convergence of the pressure distribution at the trailing edge. Using uniformly distributed collocation points in combination with a dynamic Kutta condition improves the convergence. The implementation of a C_0 transformation matrix for the multi-patch models further improves the quality of the solution.

The coupling of the aerodynamic and structural model is done through a RBF interpolation routine where the Greville abscissae are used to evaluate a set of points on both geometries to be able to achieve the interpolation. The coupling matrix is then projected back onto the control points to be able to use it for setting up the aeroelastic system. The coupling is done for two separate sets of points to ensure a realistic transfer of the aerodynamic loads onto the wingbox.

Viscous drag is estimated in a post-processing step where the 3D flow field resulting from the potential flow model is used as input for a quasi-3D boundary layer model, instead of performing complete 2D airfoil analyses. The drag estimation compares well to existing literature in terms of trends but underestimates the viscous drag by approximately 10%. This is deemed satisfactory when taking into account the scope and future application of the present computational framework.

The complete framework was demonstrated by performing an aeroelastic analysis of the uCRM wing for three different load cases. The cruise load case was used to demonstrate the aeroelastic analysis in combination with the drag estimation method. The 2.5 g symmetric pull-up and -1.0 g symmetric push-down manoeuvre load cases showed the material failure and the plate buckling analyses. Selected results were compared to results from literature and similar values were observed, confirming the capabilities of the present framework.

References

- [1] European Commission, Flightpath 2050: Europe's vision for aviation, EUR 098 EN, 2011.
- [2] J. Sobieszczanski-Sobieski, R.T. Haftka, Multidisciplinary aerospace design optimization: Survey of recent developments, *Struct. Optim.* 14 (1) (1997) 1–23. <http://dx.doi.org/10.1007/BF01197554>.
- [3] G.K.W. Kenway, J.R.R.A. Martins, Multipoint high-fidelity aerostructural optimization of a transport aircraft configuration, *J. Aircr.* 51 (1) (2014) 144–160. <http://dx.doi.org/10.2514/1.C032150>.
- [4] Z.J. Zhang, S. Khosravi, D.W. Zingg, High-fidelity aerostructural optimization with integrated geometry parameterization and mesh movement, *Struct. Multidiscip. Optim.* 55 (4) (2017) 1217–1235. <http://dx.doi.org/10.1007/s00158-016-1562-7>.
- [5] T.R. Brooks, G.J. Kennedy, J. R. R.A. Martins, High-fidelity multipoint aerostructural optimization of a high aspect ratio tow-steered composite wing, in: 58th AIAA/ASCE/AHS/ASC Structures, Structural Dynamics, and Materials Conference, American Institute of Aeronautics and Astronautics, 2017. <http://dx.doi.org/10.2514/6.2017-1350>.

- [6] A. Elham, M.J.L. van Tooren, Coupled adjoint aerostructural wing optimization using quasi-three-dimensional aerodynamic analysis, *Struct. Multidiscip. Optim.* 54 (4) (2016) 889–906. <http://dx.doi.org/10.1007/s00158-016-1447-9>.
- [7] G.J. Kennedy, J.R.R.A. Martins, A parallel aerostructural optimization framework for aircraft design studies, *Struct. Multidiscip. Optim.* 50 (6) (2014) 1079–1101. <http://dx.doi.org/10.1007/s00158-014-1108-9>.
- [8] S. Cho, S.-H. Ha, Isogeometric shape design optimization: Exact geometry and enhanced sensitivity, *Struct. Multidiscip. Optim.* 38 (1) (2008) 53–70. <http://dx.doi.org/10.1007/s00158-008-0266-z>.
- [9] T.J.R. Hughes, J.A. Cottrell, Y. Bazilevs, Isogeometric analysis: CAD, finite elements, NURBS, exact geometry and mesh refinement, *Comput. Methods Appl. Mech. Engrg.* 194 (39–41) (2005) 4135–4195. <http://dx.doi.org/10.1016/j.cma.2004.10.008>.
- [10] J.A. Cottrell, T.J.R. Hughes, Y. Bazilevs, *Isogeometric Analysis: Toward Integration of CAD and FEA*, John Wiley & Sons, 2009.
- [11] J. Kiendl, R. Schmidt, R. Wüchner, K.-U. Bletzinger, Isogeometric shape optimization of shells using semi-analytical sensitivity analysis and sensitivity weighting, *Comput. Methods Appl. Mech. Engrg.* 274 (2014) 148–167. <http://dx.doi.org/10.1016/j.cma.2014.02.001>.
- [12] A.J. Herrema, N.M. Wiese, C.N. Darling, B. Ganapathysubramanian, A. Krishnamurthy, M.-C. Hsu, A framework for parametric design optimization using isogeometric analysis, *Comput. Methods Appl. Mech. Engrg.* 316 (2017) 944–965. <http://dx.doi.org/10.1016/j.cma.2016.10.048>. Special Issue on Isogeometric Analysis: Progress and Challenges.
- [13] H. Lian, P. Kerfriden, S.P.A. Bordas, Shape optimization directly from CAD: An isogeometric boundary element approach using T-splines, *Comput. Methods Appl. Mech. Engrg.* 317 (2017) 1–41. <http://dx.doi.org/10.1016/j.cma.2016.11.012>.
- [14] K.V. Kostas, A.I. Ginnis, C.G. Politis, P.D. Kaklis, Ship-hull shape optimization with a T-spline based BEM-isogeometric solver, *Comput. Methods Appl. Mech. Engrg.* 284 (2015) 611–622. <http://dx.doi.org/10.1016/j.cma.2014.10.030>. Isogeometric Analysis Special Issue.
- [15] M.C.H. Wu, D. Kamensky, C. Wang, A.J. Herrema, F. Xu, M.S. Pigazzini, A. Verma, A.L. Marsden, Y. Bazilevs, M.-C. Hsu, Optimizing fluid-structure interaction systems with immersogeometric analysis and surrogate modeling: Application to a hydraulic arresting gear, *Comput. Methods Appl. Mech. Engrg.* 316 (2017) 668–693. <http://dx.doi.org/10.1016/j.cma.2016.09.032>.
- [16] L. Heltai, J. Kiendl, A. DeSimone, A. Reali, A natural framework for isogeometric fluid-structure interaction based on BEM-shell coupling, *Comput. Methods Appl. Mech. Engrg.* (2017). <http://dx.doi.org/10.1016/j.cma.2016.08.008>.
- [17] Z.-P. Wang, S. Turteltaub, M. Abdalla, Shape optimization and optimal control for transient heat conduction problems using an isogeometric approach, *Comput. Struct.* 185 (2017) 59–74. <http://dx.doi.org/10.1016/j.compstruc.2017.02.004>.
- [18] Y. Bazilevs, M.-C. Hsu, I. Akkerman, S. Wright, K. Takizawa, B. Henicke, T. Spielman, T.E. Tezduyar, 3D simulation of wind turbine rotors at full scale. Part I: Geometry modeling and aerodynamics, *Internat. J. Numer. Methods Fluids* 65 (1–3) (2011) 207–235. <http://dx.doi.org/10.1002/flid.2400>.
- [19] Y. Bazilevs, M.-C. Hsu, J. Kiendl, R. Wüchner, K.-U. Bletzinger, 3D simulation of wind turbine rotors at full scale. Part II: Fluidstructure interaction modeling with composite blades, *Internat. J. Numer. Methods Fluids* 65 (1–3) (2011) 236–253. <http://dx.doi.org/10.1002/flid.2454>.
- [20] E. Ferede, M.M. Abdalla, G.J.W. Van Bussel, Isogeometric based framework for aeroelastic wind turbine blade analysis, *Wind Energy* 20 (2) (2016) 193–210. <http://dx.doi.org/10.1002/we.1999>.
- [21] E. Gillebaart, R. De Breuker, Low-fidelity 2D isogeometric aeroelastic analysis and optimization method with application to a morphing airfoil, *Comput. Methods Appl. Mech. Engrg.* 305 (2016) 512–536. <http://dx.doi.org/10.1016/j.cma.2016.03.014>.
- [22] Y. Bazilevs, V.M. Calo, J.A. Cottrell, J.A. Evans, T.J.R. Hughes, S. Lipton, M.A. Scott, T.W. Sederberg, Isogeometric analysis using T-splines, *Comput. Methods Appl. Mech. Engrg.* 199 (5–8) (2010) 229–263. <http://dx.doi.org/10.1016/j.cma.2009.02.036>.
- [23] L. Piegl, W. Tiller, *The NURBS Book*, Springer Science & Business Media, 2012.
- [24] G.-D. Kim, C.-S. Lee, J.E. Kerwin, A b-spline based higher order panel method for analysis of steady flow around marine propellers, *Ocean Eng.* 34 (14–15) (2007) 2045–2060. <http://dx.doi.org/10.1016/j.oceaneng.2007.02.013>.
- [25] J. Katz, A. Plotkin, *Low-Speed Aerodynamics*, Cambridge University Press, 2001.
- [26] V. Sládek, J. Sládek, *Singular Integrals in Boundary Element Methods*, Computational Mechanics Publications, 1998.
- [27] J. Telles, Self-adaptive co-ordinate transformation for efficient numerical evaluation of general boundary element integrals, *Internat. J. Numer. Methods Engrg.* 24 (5) (1987) 959–973.
- [28] J.C.F. Telles, R.F. Oliveira, Third degree polynomial transformation for boundary element integrals: Further improvements, *Eng. Anal. Bound. Elem.* 13 (2) (1994) 135–141. [http://dx.doi.org/10.1016/0955-7997\(94\)90016-7](http://dx.doi.org/10.1016/0955-7997(94)90016-7).
- [29] E. van der Weide, G. Kalitzin, J. Schlüter, J. Alonso, Unsteady turbomachinery computations using massively parallel platforms, in: 44th AIAA Aerospace Sciences Meeting and Exhibit, American Institute of Aeronautics and Astronautics, 2006. <http://dx.doi.org/10.2514/6.2006-421>.
- [30] J. Kiendl, K.-U. Bletzinger, J. Linhard, R. Wüchner, Isogeometric shell analysis with Kirchhoff-Love elements, *Comput. Methods Appl. Mech. Engrg.* 198 (49–52) (2009) 3902–3914. <http://dx.doi.org/10.1016/j.cma.2009.08.013>.
- [31] J. Kiendl, Y. Bazilevs, M.-C. Hsu, R. Wüchner, K.-U. Bletzinger, The bending strip method for isogeometric analysis of Kirchhoff-Love shell structures comprised of multiple patches, *Comput. Methods Appl. Mech. Engrg.* 199 (37–40) (2010) 2403–2416. <http://dx.doi.org/10.1016/j.cma.2010.03.029>.
- [32] D.J. Benson, Y. Bazilevs, M.C. Hsu, T.J.R. Hughes, Isogeometric shell analysis: The Reissner–Mindlin shell, *Comput. Methods Appl. Mech. Engrg.* 199 (5–8) (2010) 276–289. <http://dx.doi.org/10.1016/j.cma.2009.05.011>.
- [33] W. Dornisch, S. Klinkel, On the choice of the director for isogeometric Reissner–Mindlin shell analysis, in: *Blucher Mechanical Engineering Proceedings*, Vol. 1, 2012, pp. 727–739.
- [34] W. Dornisch, *Interpolation of rotations and coupling of patches in isogeometric Reissner–Mindlin shell analysis*, Lehrstuhls für Baustatik und Baudynamik der RWTH Aachen, Aachen, 2015.
- [35] S.T. Ijsselmuiden, M.M. Abdalla, Z. Gürdal, Implementation of strength-based failure criteria in the lamination parameter design space, *AIAA J.* 46 (7) (2008) 1826–1834. <http://dx.doi.org/10.2514/1.35565>.
- [36] J.N. Reddy, *Mechanics Of Laminated Composite Plates and Shells: Theory and Analysis*, second ed, CRC Press, 2004.

- [37] G.J. Kennedy, G.K.W. Kenway, J.R.R.A. Martins, High aspect ratio wing design: optimal aerostructural tradeoffs for the next generation of materials, in: 52nd Aerospace Sciences Meeting, American Institute of Aeronautics and Astronautics, 2014. <http://dx.doi.org/10.2514/6.2014-0596>.
- [38] A. Khani, S.T. IJsselmuiden, M.M. Abdalla, Z. Gürdal, Design of variable stiffness panels for maximum strength using lamination parameters, *Composites B* 42 (3) (2011) 546–552. <http://dx.doi.org/10.1016/j.compositesb.2010.11.005>.
- [39] I.M. Daniel, O. Ishai, *Engineering Mechanics of Composite Materials*, Oxford University Press, 2006.
- [40] A. de Boer, A.H. van Zuijlen, H. Bijl, Review of coupling methods for non-matching meshes, *Comput. Methods Appl. Mech. Engrg.* 196 (8) (2007) 1515–1525. <http://dx.doi.org/10.1016/j.cma.2006.03.017>.
- [41] S. Shojaee, N. Valizadeh, E. Izadpanah, T. Bui, T.-V. Vu, Free vibration and buckling analysis of laminated composite plates using the NURBS-based isogeometric finite element method, *Compos. Struct.* 94 (5) (2012) 1677–1693. <http://dx.doi.org/10.1016/j.compstruct.2012.01.012>.
- [42] J. Mariens, A. Elham, M.J.L. van Tooren, Quasi-three-dimensional aerodynamic solver for multidisciplinary design optimization of lifting surfaces, *J. Aircr.* 51 (2) (2014) 547–558. <http://dx.doi.org/10.2514/1.C032261>.
- [43] A. Elham, Adjoint quasi-three-dimensional aerodynamic solver for multi-fidelity wing aerodynamic shape optimization, *Aerosp. Sci. Technol.* 41 (2015) 241–249. <http://dx.doi.org/10.1016/j.ast.2014.12.024>.
- [44] J.I. Hileman, Z.S. Spakovszky, M. Drela, M.A. Sargeant, A. Jones, Airframe design for silent fuel-efficient aircraft, *J. Aircr.* 47 (3) (2010) 956–969. <http://dx.doi.org/10.2514/1.46545>.
- [45] C.-Y. Hu, T. Maekawa, N.M. Patrikalakis, X. Ye, Robust interval algorithm for surface intersections, *Comput. Aided Des.* 29 (9) (1997) 617–627. [http://dx.doi.org/10.1016/S0010-4485\(96\)00099-1](http://dx.doi.org/10.1016/S0010-4485(96)00099-1).
- [46] J. Moran, *An Introduction to Theoretical and Computational Aerodynamics*, John Wiley & Sons, 1984.
- [47] A. van der Wees, J. van Muijden, J. van der Vooren, A fast robust viscous-inviscid interaction solver for transonic flow about wing/body configurations on the basis of full potential theory, in: 23rd Fluid Dynamics, Plasmadynamics, and Lasers Conference, in: Fluid Dynamics and Co-located Conferences, American Institute of Aeronautics and Astronautics, 1993. <http://dx.doi.org/10.2514/6.1993-3026>.
- [48] G.K.W. Kenway, G.J. Kennedy, J.R.R.A. Martins, Aerostructural optimization of the common Research Model configuration, in: 15th AIAA/ISSMO Multidisciplinary Analysis and Optimization Conference, in: AIAA AVIATION Forum, American Institute of Aeronautics and Astronautics, 2014.
- [49] T. Klimmek, Parametric set-up of a structural model for fermat configuration for aeroelastic and loads analysis, *J. Aeroelast. Struct. Dynam.* 3 (2) (2014) 31–49.
- [50] C. Kassapoglou, *Design and Analysis of Composite Structures: with Applications to Aerospace Structures*, John Wiley & Sons, 2013.
- [51] J.K.S. Dillinger, *Static Aeroelastic Optimization of Composite Wings with Variable Stiffness Laminates*, Delft University of Technology, Delft, 2014.
- [52] R.P. Liem, G.K.W. Kenway, J.R.R.A. Martins, Multimission aircraft fuel-burn minimization via multipoint aerostructural optimization, *AIAA J.* 53 (1) (2014) 104–122. <http://dx.doi.org/10.2514/1.J052940>.
- [53] N.P.M. Werter, *Aeroelastic Modelling and Design of Variable Stiffness Composite and Morphing Wings*, Delft University of Technology, Delft, 2017.